Study on the signal-to-noise ratio of Brillouin optical-time domain analyzers

SHENG WANG,[1,2] ZHISHENG YANG,[1,*] MARCELO A. SOTO,[1,3]
AND LUC THÉVENAZ[1]

[1]*EPFL Swiss Federal Institute of Technology, SCI STI LT Station 11, Lausanne CH-1015, Switzerland*
[2]*Beijing University of Posts and Telecommunications, Beijing 100876, China*
[3]*Universidad Técnica Federico Santa María, Valparaíso 2390123, Chile*
*zhisheng.yang@epfl.ch

Abstract: The signal-to-noise ratio (SNR) of Brillouin optical time-domain analyzers (BOTDA) is modelled and experimentally validated, using direct detection with and without the use of optical pre-amplification. The behavior of SNR as a function of the Brillouin gain and the probe power reaching the photo detection is analyzed in depth using this developed model and checked using two photodetectors with different specifications. It proves that a pre-amplification associated to a good-quality photodetector and a well-matched post-processing filtering can secure the highest SNR for direct-detection BOTDA. Such an optimal SNR presents only a 2.3 dB penalty compared to the ideal shot-noise-limited case that can only be reached using rather sophisticated configurations. In addition, the model here established predicts the SNR at any fiber position in any given experimental condition.

1. Introduction

Distributed optical fiber sensors have proven to be excellent tools providing unique benefits for health monitoring of large structures [1]. Among different existing techniques, Brillouin optical time-domain analysis (BOTDA) has attracted substantial attention, since it can measure environmental quantities over very long optical fibers with a spatial resolution ranging from a few centimeters up to several meters [2–4].

Studies in literature conclude that all critical specifications of BOTDA are scaled and traded-off by the signal-to-noise ratio (SNR), which represents the parameter of uttermost importance defining the overall sensing performance [5]. Any strategy increasing the signal and/or reducing the noise will therefore lead to a better performing sensor. However, the signal power cannot be infinitely increased in classical BOTDA, since the pulse duration is fixed by the required spatial resolution, whilst the maximum powers of the pulse and of the CW probe are limited by the onset of nonlinear effects [6–9]. On the other hand, the minimum noise bandwidth is determined by the targeted spatial resolution and cannot be further reduced, regardless of the denoising technique used [10]. With the increasing demand for better performance of distributed Brillouin sensors, sophisticated techniques have been proposed to further improve the SNR by enhancing the equivalent signal power, such as distributed Raman/Brillouin amplification [11–14] and/or optical pulse coding [15–20].

Nevertheless, the optimization of the detection scheme has been poorly discussed in the community so far, though it is essential to reach the best SNR and will upgrade most techniques alike. Different detection schemes have been proposed in literature, such as the use of optical pre-amplification combined with direct detection [21,22] and coherent detection [23], but it still remains unclear how large is the SNR that a given detection scheme can provide in a given configuration. Actually, as the noise in long-distance BOTDA systems is mainly determined by the detection stage [6,24], it is of crucial necessity to quantify the impact of detection schemes on the SNR of the trace. However, the BOTDA signal turns out to have its own specificity – a very small

informative modulation on top of a large non-informative continuous component – that hinders a simple extrapolation of solutions existing in different contexts, such as telecommunications and optical time-domain reflectometry where the information is contained in the full signal amplitude.

In this paper, the impact of direct detection schemes with and without the use of pre-amplification on the SNR of BOTDA measurements is thoroughly investigated. The study is performed as a function of different probe powers reaching the detection stage, regardless of the detailed sensor layout and sensing range. Analytical models for the SNR in the two detection schemes are established, and then experimentally verified using two distinct photodetectors with 3-dB bandwidths of 75 MHz and 350 MHz. Somehow counterintuitively, results show that the simple use of direct detection associated with a basic optical pre-amplification can lead to a very decent SNR, being marginally lower than the shot-noise-limited SNR usually obtained by rather sophisticated configurations.

2. General considerations on BOTDA

In a conventional BOTDA system, a high-power optical pulse – the pump – interacts with a continuous-wave signal – the probe – through stimulated Brillouin scattering [1–4]. Energy is transferred between pump and probe when the pump-probe frequency offset falls within the Brillouin gain/loss spectrum (BGS/BLS) at a given fiber location, so that the probe signal intensity in the time domain generates a trace with amplitude proportional to the local energy transfer (i.e., local Brillouin amplification/depletion). To retrieve the environmental information, the pump-probe frequency difference is scanned in order to reconstruct the local BGS/BLS, where the peak frequency, designated as Brillouin frequency shift (BFS), depends linearly on the strain and temperature applied to the fiber. Typically, the BFS distribution along the fiber is obtained by post-processing the BGS/BLS reconstructed at each fiber location [25].

In BOTDA measurements, the power of time-domain probe traces reaching the receiver, converted into the distance domain using the light group velocity, can be expressed as [5]:

$$P_s(z, v) = P_o \exp[g_B(z, v)P_{pi}\exp(-\alpha z)\Delta z] = P_o \exp[G(z, v)] \tag{1}$$

where P_o is the power of the continuous component of the probe reaching the receiver, P_{pi} is the peak power of the square-shaped pump pulse launched into the fiber, α is the fiber attenuation coefficient, $g_B(z, v)$ represents the equivalent local Brillouin gain coefficient that takes into account the mitigation of polarization fading, as well as the nonlinear effective area and the overlap of optical and acoustic modes, $G(z, v)$ is the net local Brillouin gain, and Δz is the interaction length, which is equivalent to the spatial resolution of the sensor. For meter-scale spatial resolutions and long sensing ranges (> 25 km), the local Brillouin gain $G(z, v)$ all along the fiber is typically smaller than 10% [5], so that a small-gain approximation is applicable and Eq. (1) can be rewritten as:

$$P_s(z, v) = P_o \exp[G(z, v)] \approx P_o + G(z, v)P_o \tag{2}$$

This way the converted photocurrent I_s at the photodiode output can be represented as ηP_s, where η 1 A/W is the responsivity of the photodiode. Based on Eq. (2), this photocurrent presents a large but non-informative continuous component $I_o = \eta P_o$, on top of which a small time-varying signal $I_1 = \eta G(z, v)P_o$ carries the essence of the distributed Brillouin information. As I_1 is orders of magnitude smaller than I_o, the analysis presented hereafter in this paper reasonably assumes that the sources of noise depending on the optical power (e.g., shot noise) are predominantly induced by I_o and the contributions from I_1 can be reasonably neglected.

3. Experimental setup

A standard BOTDA configuration, as shown in Fig. 1, has been implemented for this study. A distributed feedback laser diode is used as an optical source, and its output light is split

into two branches. In the upper branch, a 2-frequency probe signal is generated using an electro-optic modulator (EOM), driven by a radiofrequency (RF) signal in a suppressed-carrier double-sideband modulation scheme. Such a probe wave then passes through a polarization switch (PSw), used for polarization fading mitigation, and a variable optical attenuator (VOA) to adjust the probe power to the desired value. In the lower (pump) branch, an optical pulse of 20 ns (corresponding to 2 m spatial resolution) is generated using a semiconductor optical amplifier (SOA) followed by an EDFA. Then a VOA is used to optimize the peak pump power.
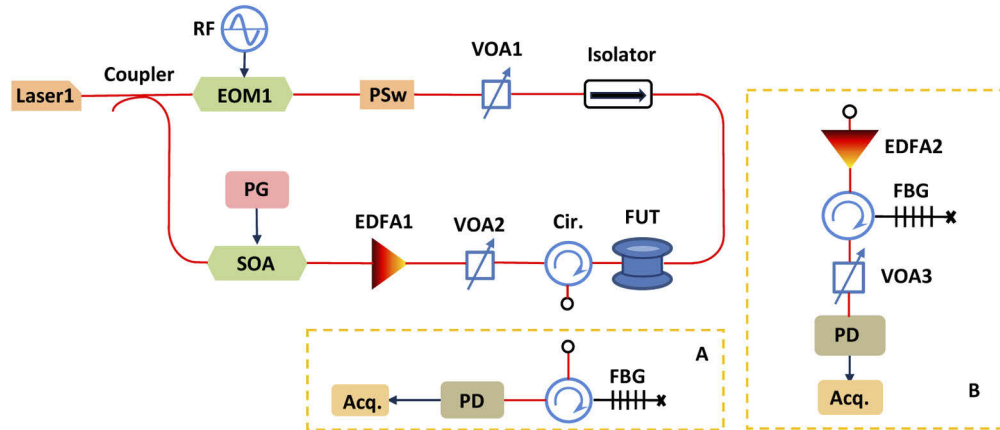

Fig. 1. Experimental test bench. EOM: electro-optic modulator; PSw.: polarization switch; VOA: variable optical attenuator; PG: pulse generator; EDFA: erbium-doped fiber amplifier; PD: photodetector; SOA: semiconductor optical amplifier; RF: radio frequency; FBG: fiber Bragg grating; FUT: fiber under test; Cir.: circulator; Acq.: acquisition.

To thoroughly investigate the SNR behavior, two standard single-mode optical fibers of 50 km and 10 km are alternatively used to cover a wide probe power range. At the detection stage, two distinct detection schemes are implemented (dotted boxes):

- Scheme A corresponds to the standard direct detection, where one sideband of the probe is selected by a narrowband FBG (6 GHz) and detected by a photodetector (PD).

- Scheme B corresponds to a direct detection with preamplification using an EDFA. In this scheme, the probe wave reaching the front-end of the detection stage is firstly amplified by an EDFA, followed by an FBG filter used to select one probe sideband and reject most of the broadband optical noise generated by the EDFA. Due to the large gain of the used EDFA, a third VOA is inserted in front of the PD to adjust the optical power just below the PD saturation.

4. SNR analysis of the conventional direct detection scheme

The first scheme analyzed here corresponds to a conventional direct detection (Scheme A in Fig. 1), with no optical pre-amplification in front of the photodetection. In this case, the detection noise is essentially composed of thermal and shot noises, causing these respective variances on the photocurrent commonly expressed as [26]:

$$\text{Thermal noise}: \quad \sigma_{th}^2 = \frac{4k_B T B_e}{R_L} \tag{3}$$

$$\text{Shot noise}: \quad \sigma_{sh}^2 = 2qI_o B_c \tag{4}$$

where k_B is the Boltzmann constant, T the absolute temperature, q is the electron charge, I_o is the photocurrent, R_L is the photo-receiver resistor providing the transimpedance conversion gain,

B_c is the detector bandwidth, and B_e is the noise equivalent bandwidth (NEB) of the thermal noise, derived from the autocorrelation function of the PD thermal noise measured in the time domain [27]. However, the thermal noise variance σ_{th}^2 described by Eq. (3) turns out to be not representative enough in most practical cases, since an electrical post-amplification stage (additional voltage amplifier after the transimpedance amplifier) present in most PDs may add an additional thermal noise. The total thermal noise must therefore be measured experimentally, represented in general as $\sigma_T^2 B_e$, where σ_T^2 is the power spectral density (PSD, in unit of A^2/Hz) of the total thermal noise (i.e., including the noise added by electrical post-amplification). In contrast, the term σ_{sh}^2 expressed by Eq. (4) is always valid for describing the shot noise. As a result, the standard deviation of the detection noise σ_N can be generalized as:

$$\sigma_N = \sqrt{\sigma_{th}^2 + \sigma_{sh}^2} = \sqrt{\sigma_T^2 B_e + 2qI_oB_c} \tag{5}$$

In order to investigate the behavior of the noise at different I_o, two common commercially available PDs with bandwidths (B_c) of 75 MHz (Thorlabs, PDB420C) and 350 MHz (Thorlabs, PDB430C), designated here as PD-75 and PD-350, are used to evaluate and verify the SNR models that will be presented hereafter. The detailed specifications of both PDs are listed in Table 1.

Table 1. Parameters of the two photodetectors used in the analysis.

Type	B_c (MHz)	B_e (MHz)	Conversion Gain (V/A)	Saturation power (dBm)	σ_T^2 (A^2/Hz)
PD-75	75	120	150000	-20	2.43e-23
PD-350	350	600	5000	-4	2.26e-22

In Table 1, the thermal noise PSD (σ_T^2) of the two photodetectors are obtained by the noise voltage measured with no light entering the photodetector. It is evident that both photodetectors include post-amplifiers because both σ_T^2 do not match with Eq. (3); more importantly, PD-350 is better performing (being less impaired by the electrical post-amplifier noise), as its σ_T^2 is only 9 times larger than that of PD-75 while its saturation power is 14 dB (25 times) higher. It suggests that a higher fraction of the conversion gain is provided by the transimpedance conversion, which is a more favorable case for noise optimization. Inserting the data from Table 1 into Eq. (5), the total noise standard deviation as a function of the input power (the optical power reaching the detection stage), is theoretically predicted for both photodetectors [blue curves in Figs. 2(a) and 2(b)], showing good agreements with the measured values (red dots). In addition, it can be seen that the thermal noise is dominant in the two detectors, while the shot noise shows only a minor contribution (3% for PD-75 and 11% for PD-350) to the total noise, even when the input optical power is close to the PD saturation.

It must be mentioned that, both the thermal and shot noise bandwidths, i.e. B_e and B_c, can be optimized (minimized) through proper post-processing (e.g., digital filtering [10]), to match the signal bandwidth B_s that is only determined by the targeted spatial resolution. This way the power of noises can be minimized. Considering only the dominant thermal noise, the noise standard deviation after bandwidth optimization could be reduced by a factor proportional to $\sqrt{B_e/B_s}$, though depending on the flatness of the thermal noise PSD in practical PDs (see details in Appendix 1). For a spatial resolution of 2 m, which will be used in experimental demonstration hereafter, the effective noise reductions are 1.9 dB and 8 dB for PD-75 and PD-350, respectively.

Combining Eq. (2) and Eq. (5), and following the definition in [5] where the SNR is defined as the ratio between the signal at the peak of the Brillouin resonance and the noise STD, the SNR of any point along the fiber can be written as:

$$SNR_{di}(z) = \frac{G_p(z)I_o}{\sqrt{\sigma_{th}^2 + \sigma_{sh}^2}} = \frac{G_p(z)I_o}{\sqrt{\sigma_T^2 B_e + 2qI_oB_c}} = G_p(z)SNR_o \tag{6}$$
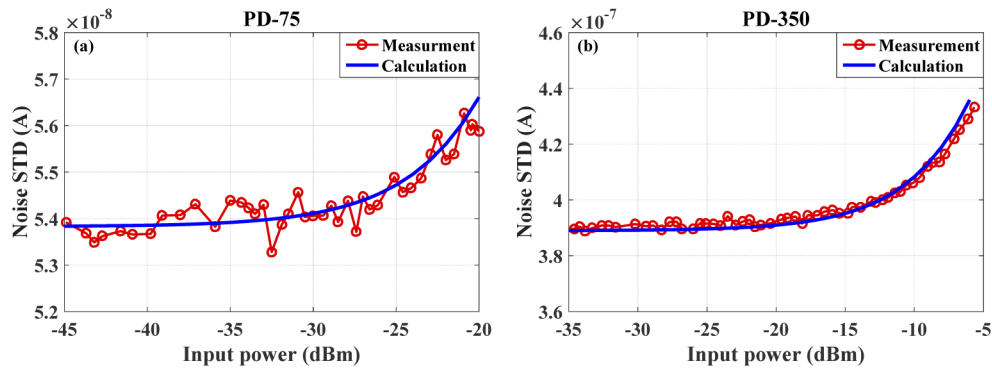
Fig. 2. Calculated and measured standard deviation of detection noises as a function of input power using (a) PD-75; (b) PD-350.

where $G_p(z)$ is the Brillouin resonance gain (i.e., peak value of the BGS) at a given fiber position. Equation (6) indicates that, for a given photoreceiver, the SNR is determined by the probe continuous component of the photo current I_o and the resonance Brillouin gain $G_p(z)$. Practically, I_o depends on the BOTDA set-up (e.g. probe power launched into the fiber and sensing range), while the Brillouin gain $G_p(z)$ in the trace depends on the Brillouin coefficient of the sensing fiber, fiber loss, spatial resolution and pump power. For simplicity and generality, the resonance Brillouin gain $G_p(z)$ is considered as a scaling factor having no connection with the detection parameters, while the SNR for $G_p(z) = 1$, designated as SNR_o and depending only on the value of I_o, is primarily investigated.

The trend of SNR_o as a function of the optical power reaching the receiver, calculated using Table 1 and Eq. (6), are shown by the dashed lines in Fig. 3 for both photodetectors. The optical power ranges from -50 dBm to -5 dBm, covering most BOTDA sensing scenarios. It can be found for both PDs that SNR_o increases with the optical power due to the dominant and signal-independent thermal noise. In addition, PD-75 always shows 8 dB higher SNR than PD-350 (before saturation) due to the narrower effective bandwidth B_e and the lower thermal noise PSD σ_T^2. For PD-75, any optical power above saturation must be attenuated down to -20 dBm, leading to an unchanged SNR_o for those powers. On the other hand, SNR_o estimated for PD- 350 continues increasing and eventually becomes larger than that of PD-75 at optical powers larger than -12 dBm. After applying a low-pass digital filtering [10] to minimize the noise bandwidths, SNR_o for both PDs are represented by the solid lines in Fig. 3. Note that PD-350 can reach a larger SNR improvement due to its larger original noise bandwidth (B_e), so that the SNR crossing point for these two photodetectors is shifted down to -18 dBm.

Knowing SNR_o, the actual SNR for a given $G_p(z)$ can be readily calculated based on Eq. (6). To verify this, theoretical SNR values obtained with two typical Brillouin gains at the fiber near-end and far-end, i.e. $G_p = 2\%$ and 0.25%, are compared with experimental results obtained with 2 m spatial resolution. For the sake of generality, the impact of trace average is normalized, i.e. all the experimental SNRs are divided by $\sqrt{n}$, where n represents the number of trace averaging. As shown in Figs. 4(a) and 4(b), the calculated (solid lines) and measured SNRs (circles) match well at different input powers. Then, by applying a digital low-pass filtering, the noise effective bandwidths B_e for both detectors are reduced to the signal bandwidth B_s (50 MHz in our case). Figures 4(c) and 4(d) show the calculated (solid lines) and measured SNRs (circles) after applying the digital filtering for the two analyzed gain values. The theoretical curves and measured SNRs are in good agreements when the input power is lower than -15 dBm, while at higher input powers the actual SNR is impaired by the beating noise between the probe wave and the spontaneous Brillouin scattering (SpBS) originating from the pump pulse, as preliminarily reported in [24].
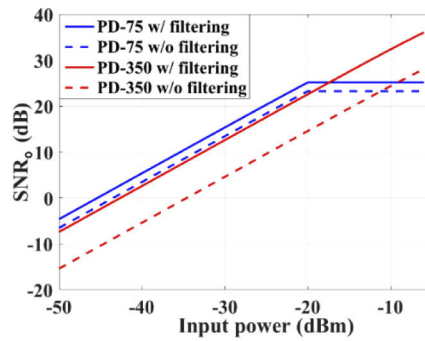
Fig. 3. The behavior of SNR_{DC} as a function of different probe power.

This SpBS-probe beating noise (see details in Appendix 2) is proportional to the probe power and the peak pump power (so indirectly related to G_p), thus the mismatch observed at high photodetector input powers is reduced for lower G_p, as shown in Fig. 4(d).
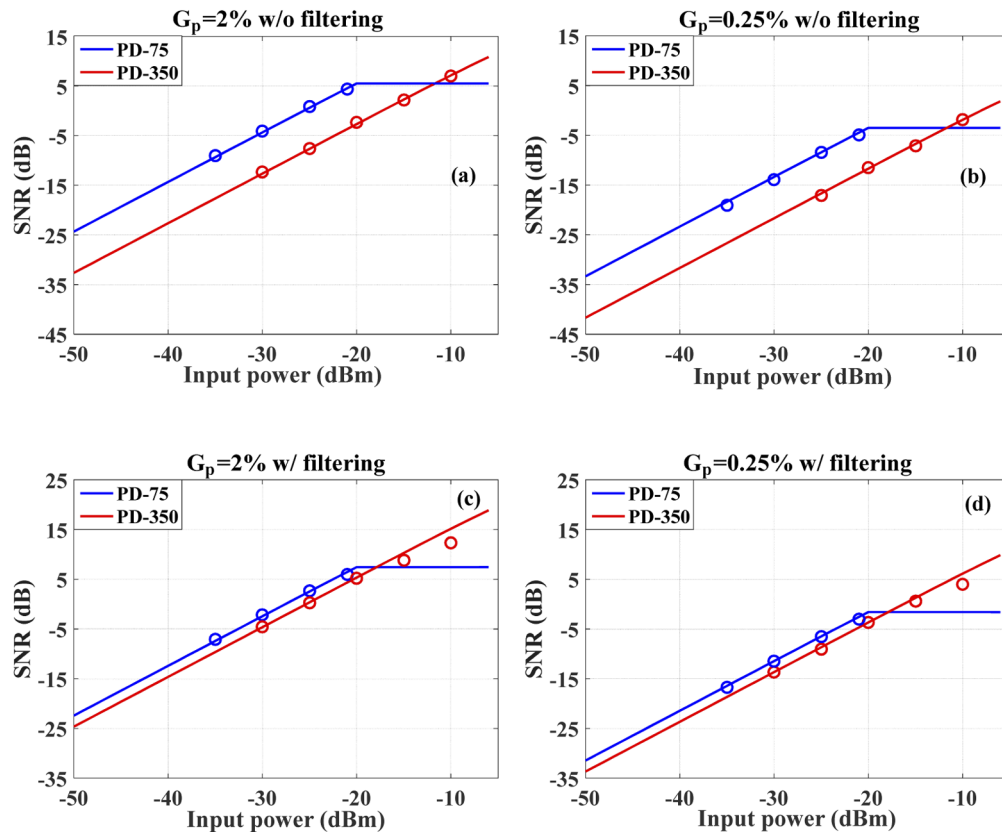

Fig. 4. The dependence of SNRs on the probe power for different resonance Brillouin gains and bandwidth optimizations: (a) 2% gain without filtering; (b) 0.25% gain without filtering; (c) 2% gain with filtering; (d) 0.25% gain with filtering.

5. Direct detection scheme with pre-amplification

From the above analysis, it can be deduced that in any case the highest SNR is obtained when the optical power entering the photodetector is near its saturation power. However, it is not possible to reach this optimal condition when the sensing distance is long and the photo detected probe power is thus much attenuated, so that an optical pre-amplifier (e.g., an Erbium-doped fiber amplifier – EDFA) is commonly inserted in front of the photodetector to enhance the measurement SNR. This optical amplification increases the detected optical signal by a factor Γ (EDFA gain), at the expense of adding amplified spontaneous emission (ASE) noise to the optical signal. This leads to a photocurrent affected by signal-ASE and ASE-ASE beating noises and their variances, respectively designated as σ^2_{s-sp} and σ^2_{sp-sp}, are expressed as [22,28]:

$$\text{Signal-ASE beating noise}: \quad \sigma^2_{s-sp} = 2F_N q(\Gamma - 1)I_\Gamma B_c \tag{7}$$

$$\text{ASE-ASE beating noise}: \quad \sigma^2_{sp-sp} = F_N^2 q^2(\Gamma - 1)^2 B_o B_c \tag{8}$$

where F_N is the noise figure of the EDFA (ideally $F_N = 2$), B_o is the optical bandwidth of ASE, and I_Γ is the continuous component of the photocurrent (being $I_\Gamma = \Gamma I_o$).

In most standard BOTDA implementations, a narrowband optical filter is placed after the EDFA to select one frequency sideband of the probe and to reduce the ASE noise. This leads to a fairly narrow optical noise bandwidth B_o, so that the contribution of σ^2_{sp-sp} can be safely neglected in all well-designed BOTDA implementations.

However, the signal-ASE beating term σ^2_{s-sp} is determined by the photodetector bandwidth B_c rather than the ASE optical bandwidth B_o, making the optical filter ineffective. As a result, in the case of direct detection together with pre-amplification, the total noise standard deviation σ_N can be eventually expressed as:

$$\sigma_N = \sqrt{\sigma^2_{th} + \sigma^2_{sh} + \sigma^2_{s-sp}} = \sqrt{\sigma_T^2 B_e + 2qI_\Gamma B_c + 2F_N q(\Gamma - 1)I_\Gamma B_c} \tag{9}$$

To validate Eq. (9), the value of the EDFA gain Γ as a function of the EDFA input power is experimentally determined using the following procedure: a continuous-wave (CW) optical signal representing the probe, ranging from -50 dBm to -5 dBm, is launched into an EDFA (with noise figure $F_N = 3$) followed by a narrow bandwidth (6 GHz) FBG filter. The optical signal filtered by the FBG is sent to an optical spectrum analyzer (OSA) to measure the amplified signal power, so that the EDFA gain Γ is determined as shown by the blue dots in Fig. 5(a). As expected, when the EDFA input power increases and reaches the EDFA saturation regime, the EDFA gain gradually decreases, since the EDFA pumping is set in constant-current mode and subsequently saturates. Note that in practice the amplified signal may saturate the photodetector in high gain (i.e., large Γ) conditions, so that a tunable attenuator is usually inserted between the FBG filter and the photodetector to set the signal power as high as possible but just below the photodetector saturation level (i.e., $I_\Gamma = I_{sat}$). Thus, the net value of Γ, including both the EDFA gain and the output attenuation, turns out to be equal to the ratio between the photodetector saturation power and the input power of the EDFA.

Based on this analysis, the actual net EDFA gain Γ used for the two photodetectors are rescaled, as shown by the red and green dots in Fig. 5(a). Using these Γ values, the standard deviation (STD) of the electrical noise as a function of the EDFA input power for both PDs are calculated based on Eq. (9), as shown by the blue curves in Figs. 5(b) and 5(c), which are in good agreement with the measured values (red dots). In the figures, the black dashed lines denote the contribution of thermal noise. It can be observed that, for both PDs, the signal-ASE beating noise I_{s-sp} dominates when the input power is low; as the input power increases, I_{s-sp} decreases and the thermal noise eventually becomes dominating.
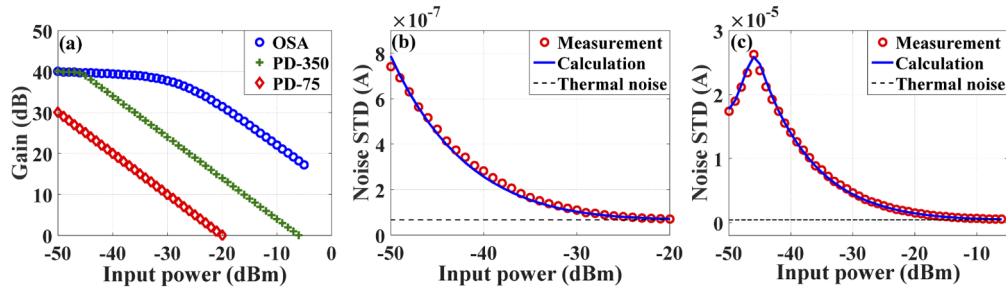
Fig. 5. (a) The gain of EDFA as a function of different input power; measured detection noise for pre-amplified direct detection using (b) PD-75; (c) PD-350.

Note that for the photodetector PD-350, the noise standard deviation grows when the input power increases from -50 dBm to -46 dBm. This feature results from the absence of photodetector saturation in this regime, so that the net gain Γ is only given by the linear-gain of the EDFA, remaining unchanged up to -46 dBm and leading to a noise level that increases with the input optical power.

Based on Eq. (9), the SNR of BOTDA traces measured by direct detection with pre-amplification can be written as:

$$SNR_{di-EDFA}(z) = \frac{G_p(z)I_\Gamma}{\sqrt{\sigma_T^2 B_e + 2qI_\Gamma B_c + 2F_N q(\Gamma - 1)I_\Gamma B_c}} = G_p(z)SNR_o \qquad (10)$$

where SNR_o represents the SNR when $G_p(z) = 1$. Figure 6(a) shows the behavior of SNR_o as a function of the input power with no digital filtering, for both PD-75 (blue solid line) and PD-350 (red solid line), respectively. Benefitting from the signal amplification, the SNR for the pre-amplified direct-detection case is always higher than that of the direct detection with no amplification [red and blue dashed lines in Fig. 6(a), obtained from Eq. (6)]. As the amplification factor G reduces as a function of the input optical power [see Figs. 5(a)–5(c)], the contribution of the thermal noise gradually increases, so that the SNR enhancement decreases accordingly.
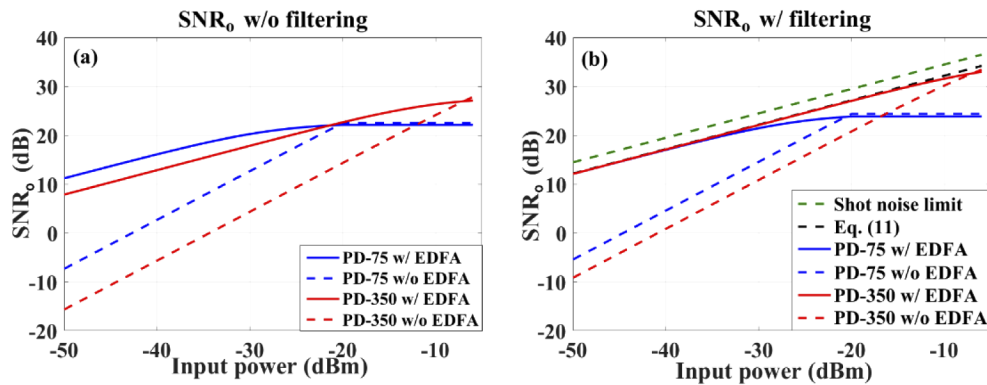

Fig. 6. (a) The behavior of SNRs as a function of different probe power (a) without filtering; (b) with filtering.

Similar to the case of direct detection, the noise bandwidth for the pre-amplified case can also be optimized to the signal bandwidth B_s by applying a post-processing filtering, such that the power of noises is minimized. The SNR behavior with post-processing filtering, in the case of 2

m spatial resolution (i.e., $B_s = 50$ MHz), is shown in Fig. 6(b) for PD-75 and PD-350, respectively. Both PDs show similar SNR performance when the EDFA input power is less than -35 dBm (i.e., when ASE-signal beating noise is dominant), so that in this regime the SNR expressed by Eq. (10) can be simplified as:

$$SNR_{di-EDFA}(z) = G_p(z)\sqrt{\frac{I_o}{2F_N q B_s}} = \sqrt{\frac{1}{F_N}} SNR_{no-EDFA}^{shot} \tag{11}$$

which is independent of any PD specifications and is represented by the black dashed line in Fig. 6(b). For a higher EDFA input power, the thermal noise becomes non-negligible, so that the difference between the real SNR and the one estimated by Eq. (11) (black dashed line) turns larger. Since the PD-350 is better performing (less impaired by post-amplification in PD), this difference is smaller than that of PD-75. Equation (11) also shows that the use of pre-amplification impairs the SNR by a factor $\sqrt{F_N}$ (2.3 dB in this case) worse than the shot noise limit [green dashed line in Fig. 6(b)]; the latter, however, might possibly be reached when using much more sophisticated detection schemes, for instance based on coherent detection.

To verify the above analysis, the measured and calculated [by Eq. (10)] SNRs are firstly compared with no post-processing filtering, for the two Brillouin gains under analysis (i.e., 2% and 0.25%), respectively, as shown in Figs. 7(a) and 7(b). For the 2% Brillouin gain, the measured SNR turns out to be slightly lower than the calculated values, which is attributed to the SpBS-probe beating noise that appears more evident in the case of higher Brillouin gain and/or
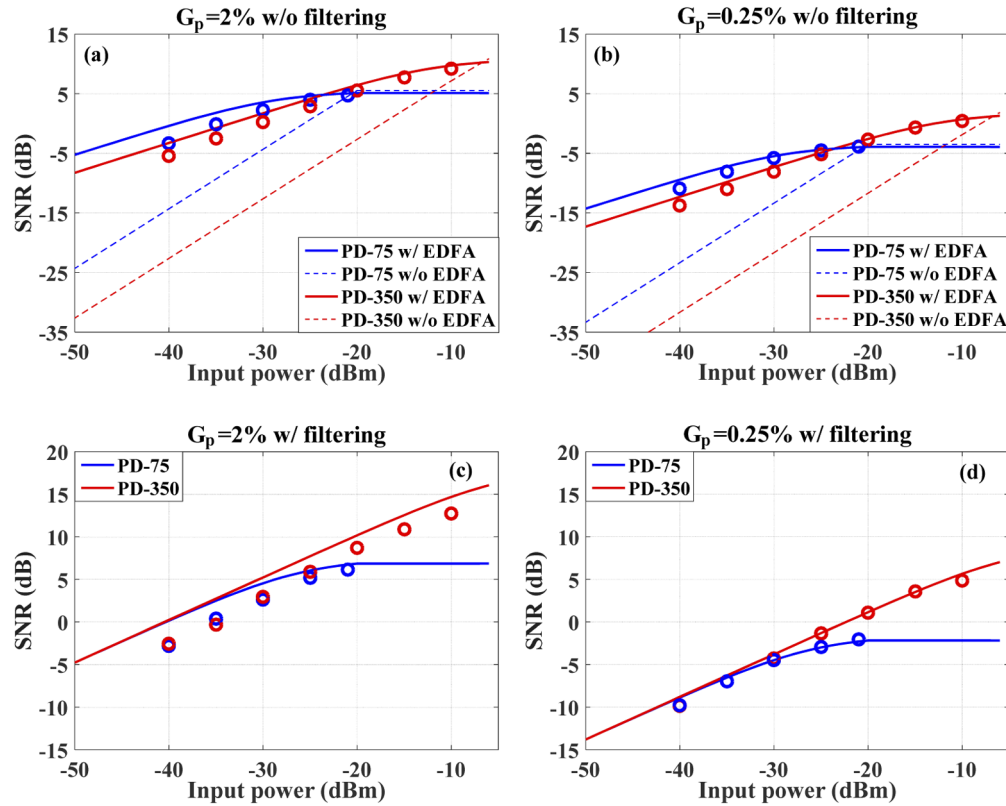

Fig. 7. The behavior of SNRs as a function of different probe power (a) 2% gain; (b) 0.25% gain; (c) 2% gain with filter; (d) 0.25% gain with filter.

lower probe power. For the 0.25% Brillouin gain, the SpBS-probe beating noise turns smaller, making the measured SNR to be much closer to the calculated values.

Figures 7(c) and 7(d) show the measured and calculated SNRs under the same previous conditions, but using a 50 MHz low-pass filter (matching the signal bandwidth with 2 m spatial resolution). It can be observed that PD-350 can always provide a similar or better SNR compared to PD-75. More specifically, both photodetectors show similar performance when the input power is lower than -35 dBm because the dominating signal-ASE beating noise is not related to the PD specifications. Applying the digital filtering, the bandwidth of signal-ASE beating noise is limited to 50 MHz, while the filter has no effect on the SpBS-probe beating noise. Thus, the SpBS-probe beating noise leads to a larger SNR degradation when compared with the non-filtered case, as shown in Fig. 7(c). For the 0.25% gain, the SpBS-probe beating noise is so low that the ASE-signal beating noise keeps dominating, leading to an SNR degradation similar to the non-filtered case, as shown in Fig. 7(d).

6. Conclusion

The behavior of the SNR has been studied and analyzed in a conventional direct-detection BOTDA scheme, with and without optical pre-amplification, leading to practical and simple expressions. The established SNR models have been experimentally validated using two typical PDs with different bandwidths. Results demonstrate that, for direct-detection BOTDA with no preamplification, the SNR depends linearly on the probe power reaching the receiver, as the thermal noise is essentially dominating and is independent of the detected signal power.

This leads to the clear conclusion that the highest SNR can be obtained by maximizing the power of the probe to be as close as possible to the photodetector saturation. This point is fundamental to reach the best operation in any configuration and for any distance range. Consequently, this indicates that the probe power launched into the sensing fiber should be set as high as possible (close to the limit of amplified spontaneous Brillouin scattering for standard BOTDA if depletion effects are mitigated [8,9]), especially in the case of long-distance sensing where the probe is much attenuated. Techniques that enable a higher probe power launched into the sensing fiber, such as probe dithering techniques [29], should be a preferred choice for long distance sensing.

When the probe power is maximized but remains far below the photodetector saturation, a preamplification stage, such as a low-noise EDFA, can be inserted just before the photodetection to further raise the SNR. In this case, since the total noise is dominated by the signal-spontaneous beating noise which depends on the signal power, the SNR grows less markedly, with a square root dependence on the probe power.

More importantly, results demonstrate that the shot-noise limit is close to be reached for any probe power using direct detection assisted by optical preamplification, by implementing a selected pre-amplifier with a low noise figure, a well-designed photodetection and a digital filtering to match noise and signal bandwidths. Such an optimized SNR can be readily estimated using Eq. (11), which offers an analytical tool to evaluate the BOTDA performance in different scenarios.

Regarding its simplicity, for instance compared to coherent detection, with no local oscillator and polarization-diversity processing, this analysis indicates that direct detection remains a very effective solution for BOTDA, which turns difficult to be decisively outperformed.

Appendix 1: Spectral behavior of the thermal noise

In this Appendix, the spectral behavior of the thermal noise is investigated, clarifying the impact of post-processing filtering on the SNR improvement [10]. Firstly, the PSDs of thermal noise for PD-75 and PD-350 are respectively measured, represented by the blue curves in Figs. 8(a) and 8(b), both exhibiting a non-uniform spectral profile. It is observed that, the frequency region with

maximal noise PSD is located around the 3-dB bandwidth of the PD (75 MHz and 350 MHz for PD-75 and PD-350, respectively), while the PSD is smaller and flatter in the low frequency region. This behavior is suspected to come from a peaking-based electronic solution in the photodetector to extend its bandwidth. So, although the post-processing filtering can minimize the thermal noise bandwidth from B_e to B_s, the noise reduction can no longer be expressed as $\sqrt{B_e/B_s}$, strictly valid for uniform PSDs. For instance, the effective noise reduction resulting from a 50 MHz low-pass filtering (corresponding to 2 m spatial resolution) is 1.9 dB and 8 dB for PD-75 and PD-350, respectively, given by the square root of the ratio between blue and red areas in Fig. 8. This has to be compared with the respective reduction of 1.9 dB and 5.4 dB for PD-75 and PD-350, respectively, assuming uniform PSDs and applying the square root law.
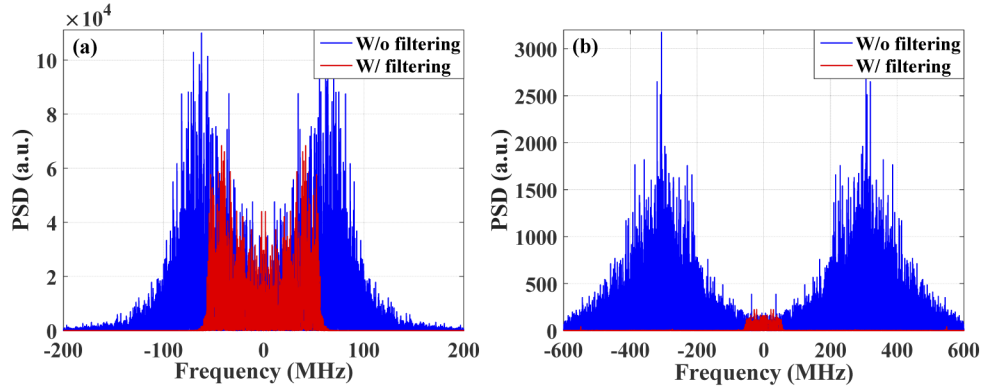

Fig. 8. Measured PSD of thermal noise of (a) PD-75; (b) PD-350.

Appendix 2: Analytical analysis of the noise caused by spontaneous Brillouin scattering (SpBS)

In this appendix, the impact of the SpBS noise on BOTDA measurements is analytically studied. Note that this effect has been observed in [24], but not yet theoretically analyzed. To estimate this noise contribution, the field amplitudes of the probe and spontaneous Brillouin scattering waves reaching the photodetector after optical pre-amplification, when the pump-probe frequency offset is close to the BFS, are described as:

$$\text{Probe wave}: \ \overrightarrow{E_s^{\Gamma}} = \hat{x}\sqrt{\Gamma}E_s \exp(j\omega_0 t) \tag{12}$$

$$\text{SpBS}: \ \overrightarrow{E_{SpBS}^{\Gamma}} = [\hat{x}\cos(\theta)\exp(j\Phi_{kx}) + \hat{y}\sin(\theta)\exp(j\Phi_{ky})]\sqrt{\Gamma}E_{SpBS}\exp(j\omega_0 t) \tag{13}$$

where E_s and E_{SpBS} are the amplitudes of probe wave and SpBS reaching the EDFA, $\hat{x}$ and $\hat{y}$ stand for the polarization direction of the probe and its orthogonal direction, respectively, the angle θ is the polarization rotation of the SpBS component with respect to the probe polarization and varies in the range $[0, \pi/2]$, Γ is the net amplification factor, including the EDFA gain and post-attenuation, and Φ_{kx} and Φ_{ky} are the random phase difference in $\hat{x}$ and $\hat{y}$ polarization direction between the SpBS signal and probe reaching the detector. This way the detected optical power can be written as:

$$P \propto (\overrightarrow{E_s^{\Gamma}} + \overrightarrow{E_{SpBS}^{\Gamma}})(\overrightarrow{E_s^{\Gamma *}} + \overrightarrow{E_{SpBS}^{\Gamma *}}) = \Gamma E_s^2 + \Gamma E_{SpBS}^2 + 2\Gamma E_s E_{SpBS}\cos(\theta)\cos(\Phi_{kx}) \tag{14}$$

Thus, the detected photocurrent, which is proportional to optical power P, can be expressed as:

$$I = \Gamma I_s + \Gamma I_{SpBS} + 2\Gamma\sqrt{I_s I_{SpBS}}\cos(\theta)\cos(\Phi_{kx}) \tag{15}$$

In Eq. (14), the first right-hand term represents the photocurrent of the BOTDA signal after pre-amplification. The second right-hand term is the photocurrent of SpBS component after pre-amplification, which is deterministic, depending on the pump power, Brillouin gain coefficient, and fiber position. Since the backscattering coefficient of SpBS in silica is around -93 dB/m [30], the typical power of the SpBS at the fiber near-end is about -70 dBm, calculated from typical injected pulse power of 20 dBm and pulse width of 20 ns. This signal decreases along the fiber distance due to the fiber attenuation, which may highly distort the measured BOTDA traces, especially at the fiber near-end and when the probe power reaching the detector is low. As experimentally demonstrated in Fig. 9(a), when the input power is -45 dBm, the trace turns out to be clearly distorted due to the superposition of the SpBS signal, and this distortion is reduced for higher input powers.
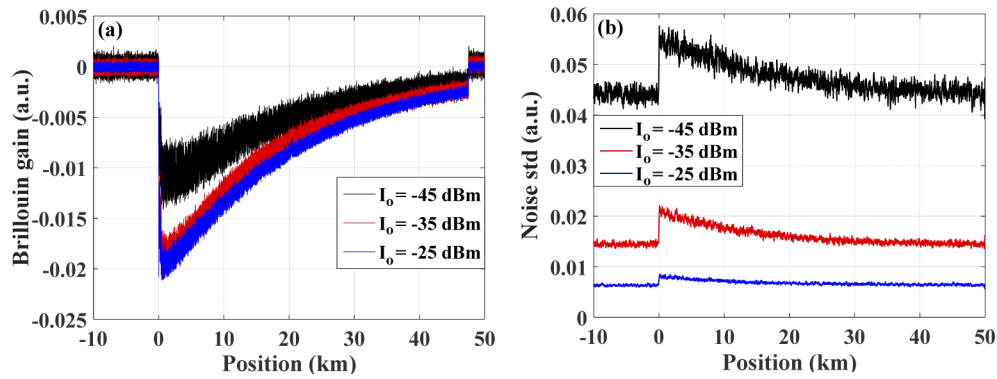

Fig. 9. (a) Brillouin loss traces after normalization; (b) the measured noise along the sensing fiber.

In Eq. (15), the third right-hand term represents the SpBS-probe beating noise, designated here as I_{SpBS-s}, which is zero-mean, and its variance can be calculated as:

$$\mathrm{var}I_{SpBS-s} = \overline{\left[2\Gamma\sqrt{I_sI_{SpBS}}\cos(\theta)\cos(\Phi_{kx})\right]^2} = \Gamma I_s\Gamma I_{SpBS} \tag{16}$$

By comparing this variance with Eqs. (7) and (9), it can be found that the signal-SpBS beating noise and signal-ASE beating noise are proportional by a factor of $I_{SpBS}/2F_NqB_c$. This means that, with a low Brillouin gain (i.e., a small I_{SpBS}), the contribution of the signal-SpBS beating component I_{SpBS-s} is negligible compared to the signal-ASE component I_{s-sp}. Figure 9(b) shows the noise STD measured along the sensing fiber at different input power, demonstrating the non-negligible impact of I_{s-sp} at the fiber near-end and its negligible impact at the fiber far-end, for any input power.

Funding

Disclosures

The authors declare that there are no conflicts of interest related to this article.

References

1. A. H. Hartog, *An introduction to distributed optical fibre sensors* (CRC, 2017).
2. T. Horiguchi, K. Shimizu, T. Kurashima, M. Tateda, and Y. Koyamada, "Development of a distributed sensing technique using Brillouin scattering," J. Lightwave Technol. **13**(7), 1296–1302 (1995).

3. A. Motil, A. Bergman, and M. Tur, "State of the art of Brillouin fiber-optic distributed sensing," Opt. Laser Technol. **78**, 81–103 (2016).

4. M. A. Soto, *Distributed Brillouin Sensing: Time-Domain Techniques* (Springer Nature Publishers, 2018).

5. M. A. Soto and L. Thévenaz, "Modeling and evaluating the performance of Brillouin distributed optical fiber sensors," Opt. Express **21**(25), 31347–31366 (2013).

6. M. Alem, M. A. Soto, and L. Thévenaz, "Analytical model and experimental verification of the critical power for modulation instability in optical fibers," Opt. Express **23**(23), 29514–29532 (2015).

7. S. M. Foaleng, F. Rodríguez-Barrios, S. Martin-Lopez, M. Gonzalez-Herraez, and L. Thévenaz, "Detrimental effect of self-phase modulation on the performance of Brillouin distributed fiber sensors," Opt. Lett. **36**(2), 97–99 (2011).

8. L. Thévenaz, S. F. Mafang, and J. Lin, "Effect of pulse depletion in a Brillouin optical time-domain analysis system," Opt. Express **21**(12), 14017–14035 (2013).

9. A. Dominguez-Lopez, Z. Yang, M. A. Soto, X. Angulo-Vinuesa, S. Martin-Lopez, L. Thévenaz, and M. Gonzalez-Herraez, "Novel scanning method for distortion-free BOTDA measurements," Opt. Express **24**(10), 10188–10204 (2016).

10. S. Zaslawski, Z. Yang, and L. Thevenaz, "On the 2D Post-Processing of Brillouin Optical Time-Domain Analysis," *J. Lightwave Technol.* (2020).

11. F. Rodriguez-Barrios, S. Martin-Lopez, A. Carrasco-Sanz, P. Corredera, J. D. Ania-Castanon, L. Thévenaz, and M. Gonzalez-Herraez, "Distributed Brillouin Fiber Sensor Assisted by First-Order Raman Amplification," J. Lightwave Technol. **28**(15), 2162–2172 (2010).

12. X. Jia, Y. Rao, C. Yuan, J. Li, X. Yan, Z. Wang, W. Zhang, H. Wu, Y. Zhu, and F. Peng, "Hybrid distributed Raman amplification combining random fiber laser based 2nd-order and low-noise LD based 1st-order pumping," Opt. Express **21**(21), 24611–24619 (2013).

13. J. Urricelqui, M. Sagues, and A. Loayssa, "Brillouin optical time-domain analysis sensor assisted by Brillouin distributed amplification of pump pulses," Opt. Express **23**(23), 30448–30458 (2015).

14. Y. H. Kim and K. Y. Song, "Tailored pump compensation for Brillouin optical time-domain analysis with distributed Brillouin amplification," Opt. Express **25**(13), 14098–14105 (2017).

15. M. A. Soto, X. Angulo-Vinuesa, S. Martin-Lopez, S. Chin, J. D. Ania-Castanon, P. Corredera, E. Rochat, M. Gonzalez-Herraez, and L. Thévenaz, "Extending the Real Remoteness of Long-Range Brillouin Optical Time-Domain Fiber Analyzers," J. Lightwave Technol. **32**(1), 152–162 (2014).

16. M. A. Soto, G. Bolognini, F. Di Pasquale, and L. Thévenaz, "Simplex-coded BOTDA fiber sensor with 1 m spatial resolution over a 50 km range," Opt. Lett. **35**(2), 259–261 (2010).

17. M. A. Soto, G. Bolognini, and F. Di Pasquale, "Long-range simplex-coded BOTDA sensor over 120km distance employing optical preamplification," Opt. Lett. **36**(2), 232–234 (2011).

18. S. L. Floch, F. Sauser, M. Llera, and E. Rochat, "Novel Brillouin optical time-domain analyzer for extreme sensing range using high-power flat frequency-coded pump pulses," J. Lightwave Technol. **33**(12), 2623–2627 (2015).

19. Z. Yang, M. A. Soto, and L. Thévenaz, "Increasing robustness of bipolar pulse coding in Brillouin distributed fiber sensors," Opt. Express **24**(1), 586–597 (2016).

20. Z. Yang, Z. Li, S. Zaslawski, L. Thévenaz, and M. A. Soto, "Design rules for optimizing unipolar coded Brillouin optical time-domain analyzers," Opt. Express **26**(13), 16505–16523 (2018).

21. S. Diaz, S. F. Mafang, M. Lopez-Amo, and L. Thévenaz, "A high-performance optical time-domain Brillouin distributed fiber sensor," IEEE Sens. J. **8**(7), 1268–1272 (2008).

22. X. Angulo-Vinuesa, A. Dominguez-Lopez, A. Lopez-Gil, J. D. Ania-Castanon, S. Martin-Lopez, and M. Gonzalez-Herraez, "Limits of BOTDA Range Extension Techniques," IEEE Sens. J. **16**(10), 3387–3395 (2016).

23. N. Guo, L. Wang, H. Wu, H. Tam, and C. Lu, "Enhanced coherent BOTDA system without trace averaging," J. Lightwave Technol. **36**(4), 871–878 (2018).

24. J. Urricelqui, M. A. Soto, and L. Thévenaz, "Sources of noise in Brillouin optical time-domain analyzers," *24th International Conference on Optical Fibre Sensors*, 9634, 963434 (2015).

25. S. M. Haneef, Z. Yang, L. Thévenaz, D. Venkitesh, and B. Srinivasan, "Performance analysis of frequency shift estimation techniques in Brillouin distributed fiber sensors," Opt. Express **26**(11), 14661–14677 (2018).

26. B. E. A. Saleh and M. C. Teich, *Fundamentals of Photonics* (John Wiley & Sons, 1991), Chap. 17.

27. R. Liao, M. Tang, C. Zhao, H. Wu, S. Fu, D. Liu, and P. P. Shum, "Harnessing oversampling in correlation-coded OTDR," Opt. Express **27**(2), 1693–1705 (2019).

28. I. Jacobs, "Dependence of optical amplifier noise figure on relative-intensity-noise," J. Lightwave Technol. **13**(7), 1461–1465 (1995).

29. R. Ruiz-Lombera, J. Urricelqui, M. Sagues, J. Mirapeix, J. M. López-Higuera, and A. Loayssa, "Overcoming nonlocal effects and Brillouin threshold limitations in Brillouin optical time-domain sensors," IEEE Photonics J. **7**(6), 1–9 (2015).

30. R. W. Boyd, *Nonlinear Optics* (Academic, 2008).